

Graph Image Prior for Unsupervised Dynamic Cardiac Cine MRI Reconstruction

Zhongsen Li, Wenxuan Chen, Shuai Wang, Chuyu Liu, Qing Zou, *Member, IEEE* and Rui Li, *Member, IEEE*

Abstract—The inductive bias of the convolutional neural network (CNN) can be a strong prior for image restoration, which is known as the Deep Image Prior (DIP). Recently, DIP is utilized in unsupervised dynamic MRI reconstruction, which adopts a generative model from the latent space to the image space. However, existing methods usually use a pyramid-shaped CNN generator shared by all frames, embedding the temporal modeling within the latent space, which may hamper the model expression capability. In this work, we propose a novel scheme for dynamic MRI representation, named “Graph Image Prior” (GIP). GIP adopts a two-stage generative network in a new modeling methodology, which first employs independent CNNs to recover the image structure for each frame, and then exploits the spatio-temporal correlations within the feature space parameterized by a graph model. A graph convolutional network is utilized for feature fusion and dynamic image generation. In addition, we devise an ADMM algorithm to alternately optimize the images and the network parameters to improve the reconstruction performance. Experiments were conducted on cardiac cine MRI reconstruction, which demonstrate that GIP outperforms compressed sensing methods and other DIP-based unsupervised methods, significantly reducing the performance gap with state-of-the-art supervised algorithms. Moreover, GIP displays superior generalization ability when transferred to a different reconstruction setting, without the need for any additional data.

Index Terms—Dynamic MRI reconstruction, cardiac cine MRI, unsupervised learning, deep image prior.

I. INTRODUCTION

Dynamic cardiac magnetic resonance imaging (MRI) is one of the most challenging problems in the field of radiology, which is constrained by the trade-off between spatial resolution and temporal resolution. To break this limit, a typical approach is to accelerate the data acquisition by skipping a part of the k-space measurements. However, k-space undersampling will lead to aliasing artifacts, which need to be removed by appropriate reconstruction algorithms.

Over the past decades, reconstructing high-quality dynamic cardiac images from undersampled measurements has been one of the most investigated topics in MRI. Many methods have been proposed to exploit the spatio-temporal redundancy within the dynamic data, including the k-t space parallel imaging methods [1], linear subspace methods [2], sparsity-based methods [3] [4], low-rank plus sparse methods [5] [6] [7], manifold-learning methods [8] [9], and many others. These methods rely on hand-crafted priors for regularizing the iterative reconstruction algorithm. The reconstruction performance is highly limited by the choice of the priors.

This work is supported by China NSFC 81971604.

Z. Li, W. Chen, S. Wang, C. Liu, and R. Li are with the school of biomedical engineering, Tsinghua University, Beijing, China. Q. Zou is with the Division of Cardiology, Department of Pediatrics, UT Southwestern Medical Center, Dallas, USA. (e-mail: leerui@tsinghua.edu.cn)

In recent years, deep learning methods have shown great potential for dynamic cardiac cine MRI reconstruction [10]. Given fully sampled data, supervised learning methods can learn to remove the aliasing artifacts and reconstruct high-quality images. Besides, deep unrolling networks mark a great advance for MRI reconstruction [11] [12] [13]. Deep unrolling methods unfold an optimization algorithm into a fixed number of iterations, alternating between the data consistency and network regularization layers [14] [15] [16]. Learnable network layers can also be used to enhance the traditional regularization priors, such as sparsity [17] and low-rankness [18] [19], which significantly improves the reconstruction performance and interpretability. However, supervised methods require ground-truth data for training, which is not always available. Besides, supervised methods often have concerns about their generalization ability.

To address these challenges, unsupervised deep-learning methods have gained increasing research focus. Recently, it is discovered that an untrained convolutional neural network (CNN) can act as a strong regularizer for image restoration, which is known as the “Deep Image Prior” (DIP) [20]. DIP is soon used in inverse problems [21] [22], and inspires several unsupervised methods for dynamic cardiac MRI reconstruction [23] [24] [25]. These methods generally adopt a generative model, which maps the latent variables to dynamic images. The mapping function is parameterized by a CNN, which is trained with the undersampled k-space data.

However, existing unsupervised dynamic cardiac MRI reconstruction algorithms based on DIP have two major limitations. First, these methods typically utilize a single pyramid-shaped CNN to parameterize the generator. Since the generator’s weights are shared across all frames, the dynamic information can only be modeled in the latent space. Existing methods often employ highly correlated low-dimensional latent variables for temporal modeling. Because the latent variables lack image structure, this model formulation may not be able to fully exploit the spatio-temporal correlations within the dynamic data. Second, current approaches generally solve the generator by directly fitting the undersampled k-space data, using the network’s output as the reconstruction result, which often leads to issues such as image blurring, over-smoothing, and loss of fine-grained details. These two limitations indicate the direction for algorithm improvements: more expressive generative models and better optimization algorithms.

In this work, we propose a novel unsupervised method for dynamic cardiac MRI reconstruction, named “Graph Image Prior” (GIP), which introduces a new generative model architecture and an ADMM algorithm for model solution. Specifically, GIP adopts a two-stage generative model. For the first stage, GIP uses independent CNNs to recover the image

structure for each frame. For the second stage, the frames are considered as vertices embedded in a graph model, and a graph convolutional network (GCN) is adopted to exploit the spatio-temporal correlations and output the dynamic images. Compared to existing methods, the central innovation of the GIP model is to exchange the order of structure-recovery and temporal-modeling in the generative process, embedding the dynamic manifold topology in the feature space. In addition, an ADMM algorithm is devised to enhance the reconstruction performance of GIP, which alternately optimizes the dynamic images and network parameters. It is important to note that this optimization algorithm fundamentally differs from the commonly used deep-unrolling networks. This algorithm does not represent a fixed number of optimizer iterations; instead, it can be iteratively performed until convergence. Moreover, after the optimization is complete, there is no need to perform an additional network inference to obtain the reconstruction results. Instead, the solution for the network parameters and dynamic images are optimized and obtained simultaneously. Our contributions can be summarized as follows:

- This work proposes a two-stage generative model to exploit the CNN structural prior for unsupervised dynamic MRI reconstruction, which innovatively models the dynamic manifold in the feature space by a graph model.
- A GCN is adopted to exploit the spatio-temporal correlations. To the best of our knowledge, this work represents the first study applying the GCN to unsupervised dynamic MRI reconstruction.
- An ADMM algorithm is devised to alternately optimize the network and images. We demonstrate by experiments that the proposed optimization algorithm can significantly improve the reconstruction performance, compared with directly fitting the k-space data.

The proposed method was validated in cardiac cine MRI reconstruction on two public datasets. Thorough experiments were conducted to compare the proposed method with several compressed-sensing (CS) methods, unsupervised methods, and supervised deep-learning methods. Experimental results demonstrate that GIP outperforms the CS methods and other unsupervised methods, and significantly reduces the performance gap with state-of-the-art supervised deep-learning methods. Moreover, GIP displays superior generalization ability when transferred to a different reconstruction setting.

II. BACKGROUND

A. Dynamic MRI Reconstruction based on DIP

The dynamic MRI acquisition can be modeled as:

$$\mathbf{y} = \mathcal{A}\mathcal{X} + \epsilon, \quad (1)$$

where $\mathcal{X} \in \mathbb{C}^{N_x \times N_y \times N_t}$ denotes the dynamic MRI images, in which N_x and N_y are the image height and width, N_t is the number of time frames. $\mathbf{y} \in \mathbb{C}^{N_s \times N_c \times N_t}$ is the multi-coil undersampled k-space data, in which N_s is the number of sample points per frame, N_c is the number of coils. $\epsilon \in \mathbb{C}^{N_s \times N_c \times N_t}$ denotes the measurement noise. $\mathcal{A} = \mathcal{F}_u \mathcal{S}$ is the multi-coil dynamic MRI system matrix, \mathcal{S} is the coil sensitivity maps, and \mathcal{F}_u is the undersampled Fourier transform.

In the generative model based on DIP, the dynamic images \mathcal{X} are considered to be generated from a latent variable \mathbf{z} :

$$\mathcal{X} = \mathbf{G}_\theta(\mathbf{z}), \quad (2)$$

where \mathbf{G}_θ is a CNN network with learnable parameters θ .

Previous studies usually use a pyramid-shaped CNN to parameterize the generator \mathbf{G}_θ , and model the dynamic information as varying but highly correlated latent variables. Yoo *et al* proposed the time-dependent DIP model (TDIP) [23], which uses a hand-crafted variable as \mathbf{z} (3-dimensional helix), and utilizes a pyramid-shaped ConvDecoder architecture [21] with a latent mapping network (MapNet) as the generator. A random temporal sliding-window sampling strategy is employed to optimize the generator from random initialization:

$$\min_{\theta} \frac{1}{K} \sum_{k=0}^{K-1} \|\mathcal{A}_k \mathbf{G}_\theta(\mathbf{z}_k) - \mathbf{y}_k\|_2^2, \quad (3)$$

where k denotes the k -th frame in the sampled batch, K is the batch size along the time dimension.

Zou *et al* proposed generative STORM (Gen-STORM) [24], which designs a regularization term to penalize the manifold distance of the generator output. Gen-STORM also adopts a pyramid-shaped CNN as the generator but utilizes transpose convolution to implement image upsampling. A progressive training-in-time approach is utilized to jointly optimize the generator and the latent variables (2-dimensional):

$$\min_{\theta, \mathbf{z}} \frac{1}{2} \|\mathcal{A} \mathbf{G}_\theta(\mathbf{z}) - \mathbf{y}\|_2^2 + \lambda_1 \|\mathcal{J}_z(\mathbf{G}_\theta(\mathbf{z}))\|_F^2 + \lambda_2 \|\nabla_t(\mathbf{z})\|_2^2, \quad (4)$$

where $\mathcal{J}_z(\cdot)$ denotes taking the Jacobian matrix respect to \mathbf{z} , $\nabla_t(\cdot)$ is the temporal finite difference operator.

Ahmed *et al* proposed a rather different generative model, named the deep bi-linear model (DEBLUR) [25], which factorizes the dynamic images into a spatial basis and a temporal basis. Two pyramid-shaped CNNs are utilized to generate the spatial and temporal components respectively, and the temporal basis is also generated from a 2-dimensional learnable latent variable. DEBLUR takes advantage of a warm-start strategy to pre-train and fine-tune the generator:

$$\begin{aligned} \min_{\theta, \phi, \mathbf{z}} \frac{1}{2} \|\mathcal{A}(\mathbf{U}\mathbf{V}^H) - \mathbf{y}\|_2^2 + \lambda_1 \|\theta\|_1 + \lambda_2 \|\phi\|_1 + \lambda_3 \|\nabla_t(\mathbf{z})\|_1, \\ \text{s.t. } \mathbf{U} = \mathbf{G}_\theta(\mathbf{U}_0), \quad \mathbf{V} = \mathbf{G}_\phi(\mathbf{z}), \end{aligned} \quad (5)$$

where \mathbf{G}_θ denotes the spatial generator, \mathbf{G}_ϕ denotes the temporal generator.

Despite the differences in algorithm details, these methods are similar in their optimization methodology, which solves the model by directly fitting the undersampled k-space data.

B. ℓ_2 -STORM for Dynamic MRI and its Relationship with Graph Model

The smooth manifold method was first introduced into dynamic cardiac MRI reconstruction as the STORM model [8], which models dynamic frames \mathcal{X}_i as points on a smooth manifold \mathcal{M} . A general formulation of the manifold methods in the continuous domain is written as:

$$f^* = \arg \min_f \sum_i \|f(\mathcal{X}_i) - \mathbf{y}_i\|^2 + \lambda \int_{\mathcal{M}} \|\nabla_{\mathcal{M}} f\|^2 d\mathcal{X}, \quad (6)$$

where $\nabla_{\mathcal{M}} f$ is the derivative of f on \mathcal{M} . For discretized MRI sampling system, the STORM method posed this penalization term as the ℓ_p -norm of the weighted distance between frames:

$$\{\mathcal{X}^*\} = \arg \min_{\mathcal{X}} \|\mathcal{A}\mathcal{X} - \mathbf{y}\|_2^2 + \lambda \sum_i \sum_j \left(\sqrt{w_{ij}} \|\mathcal{X}_i - \mathcal{X}_j\|_p \right)^p, \quad (7)$$

where the weights w_{ij} are similarity indexes computed by the distance of navigator signals d_{ij} :

$$w_{ij} = \begin{cases} e^{-(d_{ij}^2/\sigma^2)}, & \text{if } \mathcal{X}_i \text{ and } \mathcal{X}_j \text{ are neighbors.} \\ 0, & \text{otherwise.} \end{cases} \quad (8)$$

Letting $p = 2$ derives a special case of the SToRM model, ℓ_2 -SToRM, in which the manifold smoothness penalty can be further rewritten as a Tikhonov-regularization problem:

$$\{\mathcal{X}^*\} = \arg \min_{\mathcal{X}} \|\mathcal{A}\mathcal{X} - \mathbf{y}\|_2^2 + \lambda \|\mathcal{X}Q\|_2^2, \quad (9)$$

where Q is the matrix composed of the scaled eigen-vectors of the Laplacian matrix $L = QQ^H$. The Laplacian matrix L is derived from the weighting matrix $W = \{w_{ij}\}$ by $L = D - W$, where D is a diagonal matrix with entries $D(i, i) = \sum_j w_{ij}$. Also, we can utilize the matrix trace $\text{Tr}(\cdot)$ to directly regularize the problem by the Laplacian matrix:

$$\{\mathcal{X}^*\} = \arg \min_{\mathcal{X}} \|\mathcal{A}\mathcal{X} - \mathbf{y}\|_2^2 + \lambda \text{Tr}(\mathcal{X}L\mathcal{X}^H). \quad (10)$$

In fact, ℓ_2 -SToRM is equivalent to parameterizing the dynamic data structure with a weighted undirected graph model. Each frame of the dynamic data is modeled as a vertex embedded on the graph, and the matrices W , D , and L are essentially the weighted graph adjacent matrix, graph-node degree matrix, and the graph Laplacian matrix. Therefore, enforcing the Laplacian regularization term is equivalent to penalizing the off-graph components during optimization. The same optimization objective of ℓ_2 -SToRM in Eq. (10) can be derived starting from this graph model hypothesis.

The SToRM method (especially ℓ_2 -SToRM) has been demonstrated effective for dynamic MRI reconstruction in subsequent studies. The iterative SToRM method exploits the local correlations to model the manifold, which alternately updates the local graph structure and image patches, eliminating the need for navigator acquisition [26]. Besides, the kernel techniques [27], sparsity priors [28] were also introduced to the SToRM model to enhance its performance. Recently, the deep neural network was used to learn the implicit ℓ_2 -SToRM manifold structure in a data-driven manner [29].

C. Graph Convolutional Networks

Graph neural networks are proposed to handle data in non-Euclidean space. Generally, a graph can be represented as $G = (V, E, X)$, where V is the set of vertices or nodes, E is the set of edges, and X is the node feature matrix. ‘‘Graph convolution’’ indicates updating the node features by taking the weighted average of the information from the node’s neighbors [30]. Early works adopted the spectral-based method to perform graph convolution, which applies the filter in the graph Fourier space [31]:

$$X *_G g_\theta = U(U^T X \odot U^T g_\theta), \quad (11)$$

where g_θ is the parameterized graph filter, U is the matrix of eigenvectors of the graph Laplacian matrix, and $U^T(\cdot)$ is the graph Fourier transform. However, spectral-based methods need to perform eigenvalue decomposition to the graph Laplacian matrix, which is inflexible and computationally expensive.

ChebNet [32] has proved that we can use polynomials of the graph Laplacian matrix to achieve a K -order approximation

of the convolution filter, which means propagating the node information to its K -order neighborhood:

$$X *_G g_\theta = \sum_{i=0}^K \theta_i T_i(L)X, \quad (12)$$

where $T_i(L)$ is the i -order Chebyshev polynomials.

Naturally, the first-order approximation of the filter leads to the spatial-based graph convolution methods, since applying the first-order Laplacian polynomial is equivalent to utilizing the graph adjacent matrix to perform graph convolution [33]:

$$X *_G g_\theta = \hat{A}XW, \quad (13)$$

where \hat{A} is the transformed graph adjacent matrix.

Introducing non-linear activations, early GCN updates the feature matrix by a two-step graph convolution operation [33]:

$$\begin{aligned} X' &= \text{GraphConv}(X, \hat{A}, W_1, W_2) \\ &= \text{softmax}(\hat{A} \text{ReLU}(\hat{A}XW_1)W_2), \end{aligned} \quad (14)$$

where W_1 and W_2 are the transform matrix for each step.

In recent years, spatial-based GCN has become increasingly popular. The two-step graph convolution operation in Eq. (14) has been reformulated into a graph aggregate function and a graph update function, respectively [34].

$$\begin{aligned} X' &= \text{GraphConv}(X, A, W_{agg}, W_{upd}) \\ &= \text{Update}(\text{Aggregate}(X, A, W_{agg}), A, W_{upd}), \end{aligned} \quad (15)$$

where A is the graph adjacent matrix, W_{agg} and W_{upd} denote the learnable weights. The implementations of the graph aggregate function and graph update function have many choices. Operations which are order-insensitive can serve as reasonable candidates, such as averaging, pooling, etc.

Common GCNs usually utilize a pre-determined graph adjacent matrix for data mining. Recently, Han [35] proposed a learnable K -nearest-neighbor (k -NN) module to adaptively learn the graph topology, enabling broader usage of GCN without prior knowledge about the graph structure.

At present, there is very limited research utilizing the GCN for MRI reconstruction. Feng proposed to use the GCN to substitute the GRAPPA kernel for highly undersampled magnetic resonance fingerprinting reconstruction [36]. However, how to use GCN in more general MRI reconstruction applications remains a problem worth further research.

III. METHODOLOGY

A. Graph Image Prior Model

This work is motivated by the observation that existing methods for DIP-based dynamic MRI reconstruction usually adopt the ‘‘single-generator scheme’’, as shown in Figure 1(A). A single pyramid-shaped CNN is utilized for image generation shared by all the frames, transforming the latent variables to their corresponding images. Since the generator is time-independent, the temporal modeling needs to be formulated within the latent space. Therefore, highly-correlated and very low-dimensional latent variables are commonly used for generating smooth-varying dynamic movies. However, this formulation may hamper the model’s expression capability. First, the low-dimensional latent space becomes a bottleneck of the generative model, because the degree of freedom for image generation is directly restricted by latent variables regardless of the size of the generator. Second, because the latent

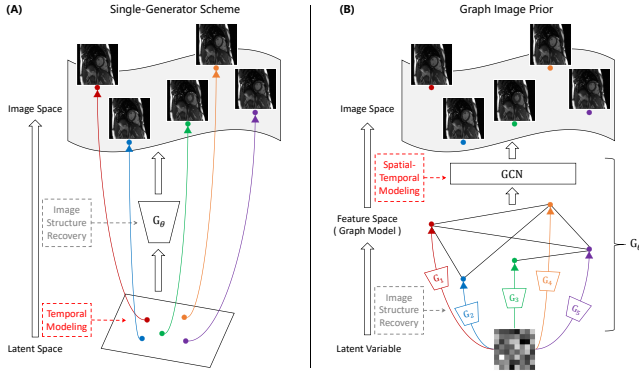


Fig. 1. The conceptual model for the single-generator scheme (A) and Graph Image Prior (B). For the single-generator scheme, a pyramid-shaped CNN shared by all frames is used for image generation. Highly correlated variables are used for temporal modeling in the latent space. In comparison, GIP exchanges the generative order and adopts a two-stage model. First, independent small CNNs G_i are used to recover the image structure for each frame. Then, each frame is considered as a node embedded in a graph, and a GCN is used for feature fusion and image generation. This strategy of modeling in feature space allows a more expressive representation in the spatio-temporal domain.

variables lack spatial structures, only temporal correlations can be modeled within the latent space. The single-generator scheme may not be able to fully exploit the spatial-temporal correlations within the dynamic MR images.

The central idea of this work is to exchange the order of the generative modeling. Specifically, we propose to formulate the model by first recovering the image structure for each frame independently, and then modeling the manifold in the feature space. Since the spatial structure is recovered at first, this model can exploit the correlations in the spatial-temporal domain. This model also eliminates the need for highly correlated latent variables because a single latent variable is enough to generate different frames via independent generators. We hypothesize that this model should be more expressive than the “single-generator scheme”.

For the first stage, we adopt an intuitive way for image recovery - allocating a separate pyramid-shaped CNN generator for each frame, which transforms the latent variable into a feature frame of image size. The second stage is of great importance for spatial-temporal manifold modeling. The ideal choice is to model all the frame-to-frame relationships, but this approach will result in a quadratic model complexity $\mathcal{O}(N_t^2)$, which brings a heavy burden for memory and computational resources. Inspired by the ℓ_2 -SToRM method [8], we adopt the graph model as the manifold representation. We treat each feature frame as a node embedded in a graph and utilize a GCN to exploit the spatial-temporal correlations. Given a fixed neighborhood size K , the model complexity can be reduced to be linear $\mathcal{O}(K \times N_t)$. We name this two-stage generative model as “Graph Image Prior” (GIP). As shown in Figure 1(B), independent CNNs ($G_i, i = 1, \dots, N_t$) are used to recover the image structure for each time frame, and then a GCN is employed for generating the dynamic images. The independent CNNs and the GCN constitute the overall generator G_θ .

B. Generator Structure

The detailed network structure of G_θ is illustrated in Figure 2. In this figure, the image size is marked by purple and the channel number is marked by blue on the right side

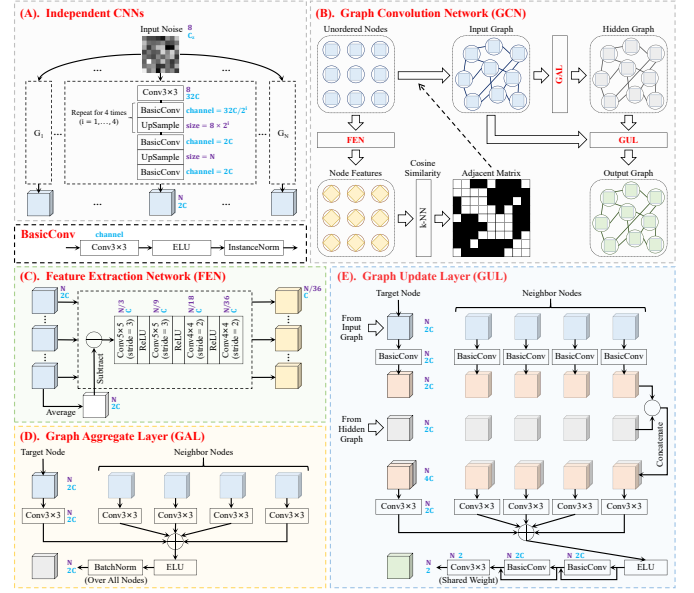


Fig. 2. The network architecture of G_θ , where the image size of the variables is marked by purple and the channel number is marked by blue. For simplicity, we use N to indicate the image of size $N \times N$. C_z is the channel number of the input latent variable. C is a hyper-parameter which controls the model capacity. (A) displays the independent CNNs ($G_i, i = 1, \dots, N_t$). (B) illustrates the GCN network, which is composed of three learnable blocks: the feature extraction network (FEN), the graph aggregate layer (GAL), and the graph update layer (GUL), as shown in (C), (D), and (E), respectively. The latent variable is first recovered to the image size for each frame by G_i . Then the GCN is utilized to adaptively determine the graph structure and exploit the spatio-temporal correlations. G_θ outputs the dynamic images of size N with 2 channels, which correspond to the real and imaginary part.

of the intermediate variables. For simplicity, we use N to indicate the image of size $N \times N$. A hyper-parameter C is used to control the model capacity. Figure 2(A) displays the structure of independent CNNs ($G_i, i = 1, \dots, N_t$). A 2D noise latent variable of size 8×8 and C_z channels is input into G_i to recover the image structure. Each feature frame output from G_i has the image size $N \times N$ and $2C$ channels. Figure 2(B) illustrates the GCN network, which is composed of three learnable blocks: the feature extraction network (FEN), the graph aggregate layer (GAL), and the graph update layer (GUL), as shown in (C), (D), and (E), respectively. In order to formulate this model for the most general dynamic MRI reconstruction problem, we do not make any prior assumptions about the graph structure or utilize any navigator data to pre-estimate the adjacent matrix. Instead, we employ the learnable k-NN strategy proposed in [35] to adaptively learn the graph topology from the dynamic data itself. First, the FEN is used to perform pooling on the feature frames to obtain low-dimensional node features. Then, cosine-similarity matrix is calculated between the node features, and the kNN algorithm is employed for clustering the neighbors and producing the graph adjacent matrix. Next, the unordered nodes generated from the independent CNNs are connected into the input graph, where the number of vertices equals the number of frames. Afterwards, the GAL is used to synthesize the neighborhood information for each node, which establishes a hidden graph containing the aggregated features. The mean aggregator is adopted as the graph aggregate function. Finally, the GUL receives both the input graph and the hidden graph

to update the features for each graph node. We follow the popular update function which concatenates the graph node with its aggregate features, and employ a weighted-average update function [34]. At the output layer of GUL, the channel number is reduced to 2, which corresponds to the real and imaginary part of complex-valued dynamic images.

C. Optimization Algorithm

Although the GIP generator is effective for exploiting the spatio-temporal correlations, its reconstruction performance may be limited by the strong structural bias of CNN. Inspired by Lu's work [37], we devise an ADMM algorithm to alternately optimize the dynamic images and the network parameters to further improve the reconstruction performance.

We first consider the following optimization problem:

$$\min_{\mathcal{X}, \theta} \frac{1}{2} \|\mathcal{A}\mathcal{X} - \mathbf{y}\|_2^2, \quad \text{s.t. } \mathcal{X} = \mathbf{G}_\theta(\mathbf{z}), \quad (16)$$

where \mathbf{G}_θ denotes GIP generator, \mathbf{z} denotes the latent variable. The equation constraint of this problem enforces that the reconstructed dynamic images are the output from the GIP generator \mathbf{G}_θ . To relax this constraint, we form the augmented Lagrangian associated with Eq. (16) as follows:

$$\min_{\mathcal{X}, \theta} \frac{1}{2} \|\mathcal{A}\mathcal{X} - \mathbf{y}\|_2^2 + \frac{\rho}{2} \|\mathcal{X} - \mathbf{G}_\theta(\mathbf{z})\|_2^2 + \mathbf{Re}(\langle \Lambda, \mathcal{X} - \mathbf{G}_\theta(\mathbf{z}) \rangle), \quad (17)$$

where ρ denotes the relaxation coefficient, Λ is the Lagrangian multiplier, $\mathbf{Re}(\cdot)$ denotes taking the real part.

Next, we adopt the ADMM algorithm to solve Eq. (17):

$$\begin{aligned} \mathcal{X}^{(k)} &= \min_{\mathcal{X}} \frac{1}{2} \|\mathcal{A}\mathcal{X} - \mathbf{y}\|_2^2 + \frac{\rho}{2} \|\mathcal{X} - \mathbf{G}_{\theta^{(k-1)}}(\mathbf{z})\|_2^2 \\ &\quad + \mathbf{Re}(\langle \Lambda^{(k-1)}, \mathcal{X} - \mathbf{G}_{\theta^{(k-1)}}(\mathbf{z}) \rangle), \\ \theta^{(k)} &= \min_{\theta} \frac{\rho}{2} \left\| \mathcal{X}^{(k)} - \mathbf{G}_\theta(\mathbf{z}) \right\|_2^2 \\ &\quad + \mathbf{Re}(\langle \Lambda^{(k-1)}, \mathcal{X}^{(k)} - \mathbf{G}_\theta(\mathbf{z}) \rangle), \\ \Lambda^{(k)} &= \Lambda^{(k-1)} + \rho(\mathcal{X}^{(k)} - \mathbf{G}_{\theta^{(k)}}(\mathbf{z})). \end{aligned} \quad (18)$$

Note that the first step of Eq. (18) has a closed-form solution by taking the derivative to zero, leading to a linear equation with a symmetric positive definite system matrix:

$$\mathcal{X}^{(k)} = (\mathcal{A}^H \mathcal{A} + \rho \mathbf{I})^{-1} (\mathcal{A}^H \mathbf{y} + \rho \mathbf{G}_{\theta^{(k-1)}}(\mathbf{z}) - \Lambda^{(k-1)}), \quad (19)$$

which can be solved efficiently by the conjugate-gradient descent (CG) algorithm.

The second step of Eq. (18) is a minimization problem of a quadratic form about $\mathbf{G}_\theta(\mathbf{z})$. If we omit the irrelevant terms with $\mathbf{G}_\theta(\mathbf{z})$, this step can be simplified to:

$$\theta^{(k)} = \min_{\theta} \left\| \mathbf{G}_\theta(\mathbf{z}) - \left(\mathcal{X}^{(k)} + \frac{1}{\rho} \Lambda^{(k-1)} \right) \right\|_2^2. \quad (20)$$

Interestingly, this optimization objective is exactly a minimization problem about the output of the generator \mathbf{G}_θ . Therefore, we can solve this sub-problem by network training using the back-propagation algorithm.

D. Pretraining Strategy

Because the objective in Eq. (17) is non-convex, convergence to the global minima cannot be guaranteed with the ADMM algorithm. Therefore, appropriate initialization of \mathbf{G}_θ is critical for a good solution. In this work, we adopt a three-stage pretraining strategy to find a good initialization for \mathbf{G}_θ . It

Algorithm 1 Proposed GIP Reconstruction Framework

Input:

The acquired k-space measurements \mathbf{y} .
The dynamic MRI encoding system matrix $\mathcal{A} = \mathcal{F}_u \mathcal{S}$.
A GIP generator \mathbf{G}_θ .
A 2D multi-channel latent variable \mathbf{z} .

Initialization:

Randomly initialize the parameters $\theta = \{\theta_G, \theta_{GCN}\}$.
Randomly initialize \mathbf{z} (Gaussian distributed).

Pretraining:

Pretraining of θ_G using Eq. (21).
Pretraining of θ_{GCN} using Eq. (22).
Pretraining of θ using Eq. (23).

ADMM Optimization:

Hyper-Parameters: ρ, N_{ADMM} .
Variables: $\theta^{(0)}$ (pretrained), $\mathcal{X}^{(0)} = \mathbf{G}_{\theta^{(0)}}(\mathbf{z})$, $\Lambda^{(0)} = 0$.
for $k = 1$ to N_{ADMM} **do**
 Update of $\mathcal{X}^{(k)}$ using Eq. (19).
 Update of $\theta^{(k)}$ using Eq. (20).
 Update of $\Lambda^{(k)}$ using:
 $\Lambda^{(k)} = \Lambda^{(k-1)} + \rho(\mathcal{X}^{(k)} - \mathbf{G}_{\theta^{(k)}}(\mathbf{z}))$.

end

Output: Dynamic images $\hat{\mathcal{X}} = \mathcal{X}^{(k)}$, parameters $\hat{\theta} = \theta^{(k)}$.

should be stressed that each pretraining stage also only utilizes the undersampled k-space data, and does not need the help of any other reconstruction methods. Therefore, the overall optimization process of \mathbf{G}_θ from random initialization to the final solution is purely unsupervised, including the pretraining stage and the proposed ADMM algorithm.

Since the GIP generator \mathbf{G}_θ has two parts - the independent CNNs ($G_i, i = 1, \dots, N_t$) and the GCN, we also divide the parameters θ into $\theta = \{\theta_G, \theta_{GCN}\}$. The pretraining of \mathbf{G}_θ consists of the following three stages: pretraining θ_G , pretraining θ_{GCN} , and fine-tuning the overall θ .

For the first stage, we add an extra convolution layer C_i at the end of each CNN G_i , to reduce the feature frame channels to 2. This extra layer C_i with learnable parameters θ_{C_i} is only used in this pretraining stage and will be discarded for the subsequent algorithm steps. In this way, we can initialize θ_G by fitting the undersampled k-space data:

$$\min_{\theta_G, \theta_C} \sum_{i=1}^{N_t} \|\mathcal{A}_i C_i(G_i(\mathbf{z})) - \mathbf{y}_i\|_2^2. \quad (21)$$

For the second stage, we fix the weights θ_G initialized in the previous stage, and pretrain the GCN by fitting the undersampled k-space data:

$$\min_{\theta_{GCN}} \|\mathcal{A} \mathbf{G}_{\theta}(\mathbf{z}) - \mathbf{y}\|_2^2. \quad (22)$$

Finally, after θ_G and θ_{GCN} both find a good initialization, we conduct the third stage pretraining to fine-tune all the parameters in the GIP generator:

$$\min_{\theta} \|\mathcal{A} \mathbf{G}_{\theta}(\mathbf{z}) - \mathbf{y}\|_2^2. \quad (23)$$

The graph adjacent matrix determined by the pretraining is fixed for the following ADMM algorithm. The overall reconstruction algorithm of the GIP model is shown in **Algorithm 1**.

IV. EXPERIMENTAL SETUPS

A. Dataset and Preprocessing

Two cardiac cine MRI datasets were used in this work.

The first is the Ohio OCMR dataset [38]. A total of 76 fully sampled dynamic data slices from 43 different subjects were included in the experiment dataset. The coil number is compressed to 8 by the GCC algorithm [39]. The slices are all cropped to the image size 192×144 . We divided the data into three groups: 60 slices for training, 6 slices for validation, and 10 slices for testing. Besides, we applied data augmentation by cropping the slices to image size 144×144 at stride 12, which finally produced 300 slices for training, 30 slices for validation, and 50 slices for testing.

The second is the Siemens CMRxRecon dataset [40]. It contains 119 fully sampled multi-coil cardiac MRI cases. Each data has 12 frames and 10 coils. For each case, the central 3 slices at the middle position are included in the experiment dataset, which produces 357 dynamic slices. We cropped the image size to 192×192 , and divided the data into 240 slices for training, 30 slices for validation, and 87 slices for testing.

The ESPIRiT algorithm [41] was used to calculate the coil sensitivity maps. A 32×32 block at the center of the time-averaged k-space data (ACS data) is used for calibration.

B. Algorithms and Experimental Details

In this work, we implemented ℓ_2 -SToRM, two CS methods (L+S [7] and k-t SLR [6]), four supervised deep-learning methods (CRNN [15], SLR-net [18], CTF-net [16] and L+S-net [19]), and two unsupervised methods (TDIP [23] and GenSToRM [24]) for comparison. All methods were implemented according to the source code provided by the authors. However, since the view-sharing strategy is not compatible with Cartesian sampling, the training strategy of TDIP and GenSToRM needs necessary modifications. To ensure a reliable comparison, we adopted the training strategy suggested by the authors, making the minimum changes to adapt the algorithms to arbitrary sampling patterns. For TDIP, we use random batch sampling among the time frames to train the generator, instead of sampling from all possible sliding windows [23]. For GenSToRM, we adopt a two-stage progressive training-in-time approach [24], which first initializes the generator by fitting the time-averaged k-space data and then fine-tune the parameters by training on the undersampled dynamic data.

For the supervised deep-learning methods, we directly used the default network architecture released by the authors. All the supervised methods were trained on the OCMR training set by the Adam optimizer with a learning rate $lr=5 \times 10^{-4}$ and $\beta=(0.9, 0.999)$. The mean squared error was used as the loss function. Random patch sampling is adopted along the time dimension to generate training samples of size $144 \times 144 \times 20$. 100 epochs were used for training to ensure complete convergence. Validation was performed after each epoch and the best model on the validation set was saved for testing. The trained model was tested by reconstructing a dynamic slice without temporal patch sampling.

For the CS methods and unsupervised methods, we adjusted their parameters on the OCMR validation set to ensure their best performance. For TDIP, we adopted the ‘‘Helix (L=3)

+ MapNet (L=64)’’ as the latent space design, which was reported to achieve the best performance [23]. For GenSToRM, we fixed the latent dimension $l(z) = 2$ and model parameter $d = 24$ as suggested by the authors [24].

The reconstruction methods were implemented in PyTorch on an Ubuntu 20.04 LTS operating system equipped with 8 NVIDIA A800 GPUs. In the spirit of reproducible research, we have open-sourced our code and all implementation details at https://github.com/lizs17/GIP_Cardiac_MRI.

C. Evaluation Metrics

We used four quantitative metrics to provide a comprehensive evaluation of the reconstruction performance: mean square error (MSE), peak signal-to-noise ratio (PSNR), structural similarity index (SSIM), and mean absolute error (MAE):

$$\begin{aligned} \text{MSE} &= \frac{1}{M} \|\hat{x} - x^*\|_2^2, \\ \text{PSNR} &= 10 \log_{10} \left(\frac{M}{\|\hat{x} - x^*\|_2^2} \right), \\ \text{SSIM} &= \mathbf{1}(\hat{x} - x^*) \cdot \mathbf{c}(\hat{x} - x^*) \cdot \mathbf{s}(\hat{x} - x^*), \\ \text{MAE} &= \frac{1}{M} \|\hat{x} - x^*\|_1. \end{aligned} \quad (24)$$

where x^* is the ground-truth image and \hat{x} is the reconstructed image, M is the total number of image pixels. Details about the SSIM index are shown in [42]. The metrics are evaluated for each frame independently and then averaged to give the final value for the dynamic reconstruction. Besides, the unit for each metric is adjusted to ensure an appropriate value range: MSE ($\times 10^{-5}$), PSNR (dB), SSIM (%), MAE ($\times 10^{-3}$).

V. EXPERIMENTS AND RESULTS

A. Effect of Algorithm Parameters

In this study, we investigated the influence of the algorithm hyper-parameters, which are divided into two categories:

1) *Network Parameters*: the parameters of \mathbf{G}_θ , including the network size parameter C , the latent variable channels C_z , and the number of neighbors K . Since a prohibitively long time is required to conduct a grid search over all parameter combinations, we empirically fixed the parameter $K=5$, and performed a grid search on $C \in \{4, 8, 12, 16, 20, 24, 28, 32\}$ and $C_z \in \{1, 2, 4, 8, 16, 32, 64, 128\}$. After C and C_z are determined, we varied $K \in \{2, 3, 4, 5, 6, 7, 8, 9\}$ to identify the best K value.

The results on the network parameters are shown in Figure 3. We observed in Figure 3(A) that when C and C_z are too small, the reconstruction performance is limited by the capacity of the generative model. The PSNR of the reconstructed image gradually increases with C and C_z . This trend is approximately stopped at $C = 12$ and $C_z = 8$, after which the reconstruction performance seems to reach saturation, forming a plateau on the 3D landscape. Therefore, we set $(C, C_z) = (12, 8)$ as the best parameter. The results about K are shown in Figure 3(B). The reconstruction performance increases nearly monotonically with K . The turning point occurs at $K = 7$, which is selected as the best value.

2) *ADMM Parameters*: the parameters of the ADMM algorithm. For each iteration, we used 10 CG steps and adopted the Adam optimizer with learning rate $lr=1 \times 10^{-5}$ and $\beta=(0.5, 0.98)$ to train \mathbf{G}_θ with 500 iterations. We mainly investigated the influence of two parameters: the number of

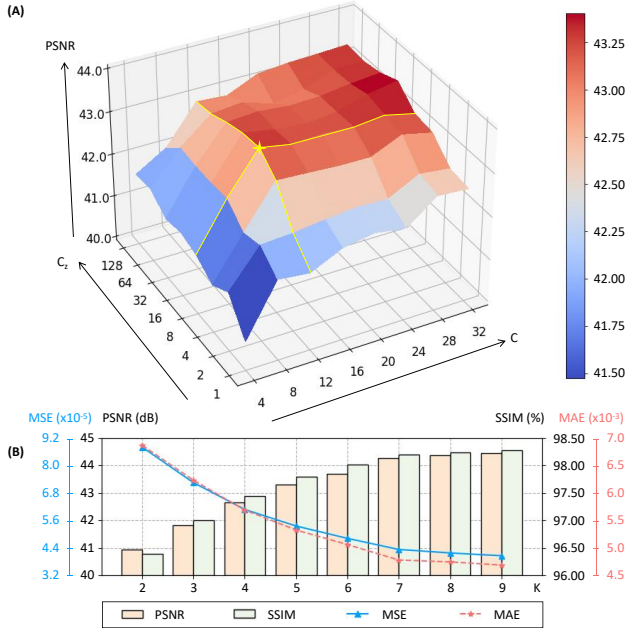


Fig. 3. Experiment results on the influence of network parameters. (A) displays the 3D landscape of the reconstructed image PSNR, calculated from the parameter grid search about C and C_z . The yellow star marks the choice of the optimal parameters, which correspond to $C = 12$ and $C_z = 8$. Experiment results on the influence of K are shown in (B).

ADMM iterations, and the relaxation parameter ρ . We varied $\rho \in \{0.0001, 0.0005, 0.001, 0.005, 0.01, 0.05, 0.1\}$, and set the ADMM iterations to 50. The reconstructed images (including $G_\theta(z)$ and \mathcal{X}) are evaluated for each ρ and every iteration.

The results on the iteration parameters are shown in Figure 4. Figure 4(A) depicts the MSE and PSNR curves, which demonstrates that the ADMM algorithm comes to convergence as the iteration progresses. Besides, the image quality improvement of \mathcal{X} is closely accompanied by $G_\theta(z)$, indicating that the image \mathcal{X} and network parameters θ are indeed optimized simultaneously. The MSE curves under different ρ settings are shown in (B). When ρ is too large ($\rho=0.1$), the algorithm convergence will be significantly slowed down. When ρ is too small ($\rho=0.0001$), the convergence also becomes slower, and the final solution seems to be worse. We fix the iterations to 20 and calculate the quantitative metrics under different ρ values, as shown in (C), from which we select the best $\rho=0.001$.

B. Reconstruction Performance

The algorithms were adjusted to their best performance and evaluated on the OCMR dataset. 2D random Poisson masks are used for k-space sampling, which varies with different frames and the center region is fully sampled (ACS signals). Experiments were conducted under two acceleration settings ($R=8.0$, $ACS=[10,10]$) and ($R=16.0$, $ACS=[6,6]$).

The reconstructed images of a representative case are shown in Figure 5. At $R=8.0$, L+S and k-t SLR can both produce good image quality. A relatively higher reconstructed error occurs at the blood-myocardium boundary. The supervised learning algorithms all achieve excellent reconstruction accuracy with very low error levels. For the unsupervised methods, TDIP and GenSToRM produce worse reconstruction quality, even compared with the CS methods. In comparison, the proposed GIP method achieves comparable reconstruction accuracy with the supervised methods, producing a uniform

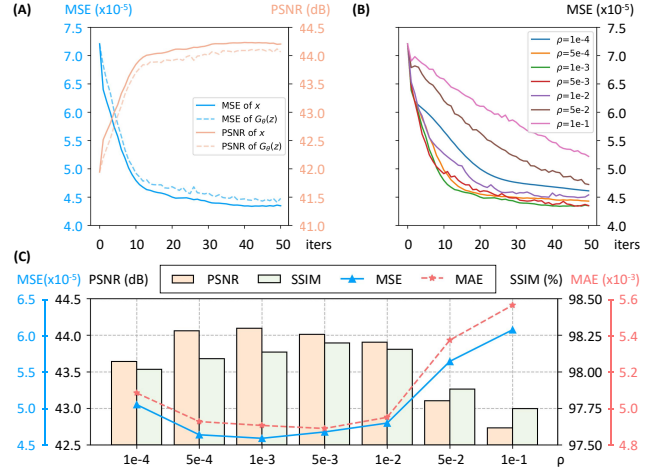


Fig. 4. Experiment results on the influence of iteration parameters. (A) displays the MSE and PSNR curves related to the iteration steps, in which the reconstructed image x is plotted by the solid line, and the generated image $G_\theta(z)$ is plotted by the dotted line. The MSE-iteration curves under different ρ settings are shown in (B). The reconstruction performance under different ρ settings are shown in (C).

error map. At $R=16.0$, since fewer measurements are available, the reconstruction performances of all the algorithms decrease. Tiny structures are easily lost or blurred during reconstruction at such a high acceleration factor, especially for algorithms based on low-rank priors. However, as marked by the red arrows on the image and the white arrows on the error map, GIP achieves high reconstruction fidelity of the small details.

Table I summarizes the quantitative results. We noticed that the supervised methods lead the first-level reconstruction performance at both acceleration settings, in which the L+S-net achieves the best results. The CS methods have a performance gap with the supervised methods, approximately 5dB in PSNR compared with the L+S-net method. The TDIP and GenSToRM methods display even worse performance compared with the CS methods. In comparison, the proposed GIP method significantly outperforms other CS and unsupervised methods, greatly reducing the gap with the supervised methods. The computational time of different reconstruction methods is summarized in Table III.

C. Generalization Performance

We compared the generalization ability of the reconstruction methods when they were transferred to a different dataset. We fixed the parameters adjusted in the OCMR dataset, and directly applied all the methods to reconstruct the CMRxRecon test set. 2D Poisson sampling with two acceleration settings ($R=8.0$, $ACS=[12,12]$) and ($R=16.0$, $ACS=[8,8]$) are evaluated.

Table II shows the quantitative results of the generalization experiment. The performance of the CS methods remains relatively stable when the dataset is changed. However, performance degradation occurs in all supervised algorithms, though most of them are still better than the CS methods. In comparison, GIP displays superior generalization performance, achieving the best score on all the quantitative metrics.

D. Ablation Experiments

We conducted ablation experiments to validate the effectiveness of the key components in the GIP method: the GCN network and the ADMM optimization algorithm. Specifically, we use “DIP only” to indicate that only the independent

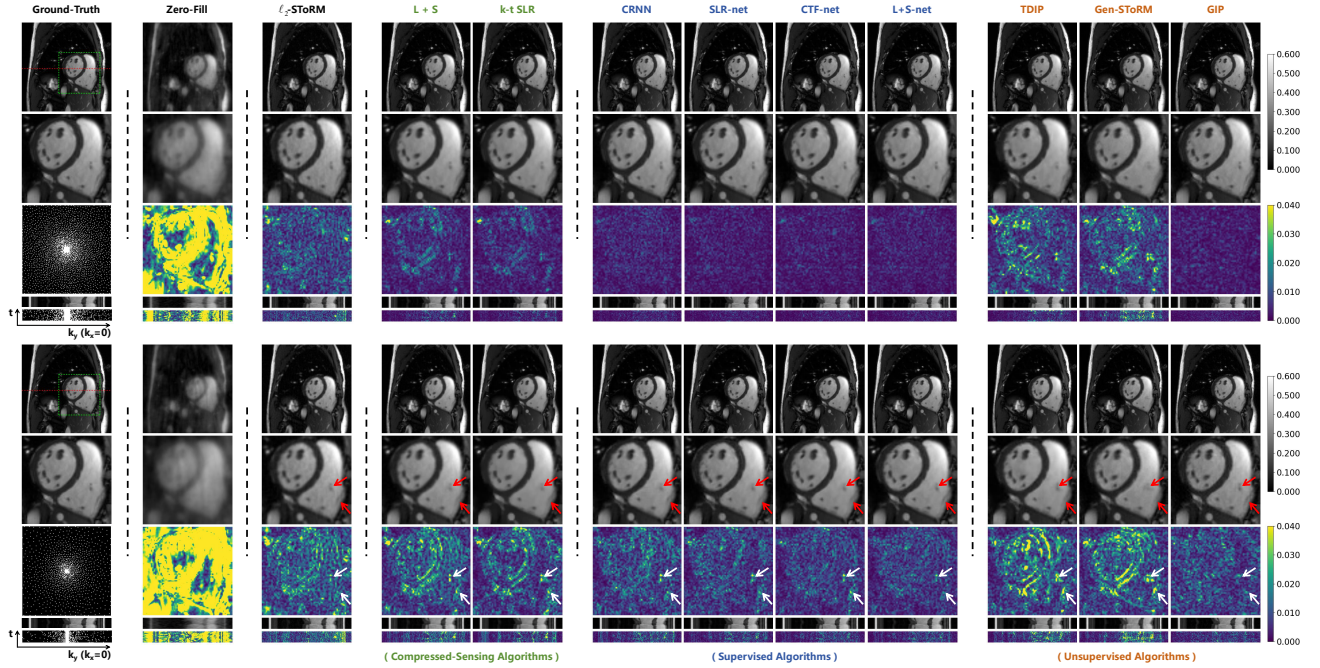


Fig. 5. The reconstruction results of a case in the OCMR dataset. The upper half shows the results of $R=8.0$ and the lower half shows $R=16.0$. The first row displays, from left to right, the ground truth and the reconstructed images. The second row shows the zoomed-in image of the heart regions, framed by the green box. The third row shows the undersampling mask and the reconstruction error maps. The fourth row shows the y -t motion profile (plotted at the red line) and the corresponding error maps. The ky -t sampling pattern is plotted at the left-bottom corner. The grayscale range and error color bar are shown on the right side. The arrows mark the small papillary muscles and tendons on the heart.

TABLE I

QUANTITATIVE RESULTS ON THE OCMR DATASET (MEAN \pm STANDARD DEVIATION).

Metrics	Compressed-Sensing			Supervised				Unsupervised			
	ℓ_2 -StoRM	L+S	k-t SLR	CRNN	SLR-net	CTF-net	L+S-net	TDIP	Gen-StoRM	GIP	
$R=8.0$	MSE	7.42 \pm 2.15	2.25 \pm 1.10	2.21 \pm 0.92	1.18 \pm 0.70	0.95 \pm 0.54	0.83 \pm 0.48	0.75\pm0.43	4.63 \pm 2.35	6.64 \pm 3.47	0.98 \pm 0.45
	PSNR	41.66 \pm 1.54	47.30 \pm 2.57	47.15 \pm 2.09	50.27 \pm 3.01	51.11 \pm 2.85	51.82 \pm 3.06	52.14\pm2.92	44.76 \pm 2.57	42.73 \pm 2.44	50.63 \pm 2.08
	SSIM	96.37 \pm 1.17	99.22 \pm 0.32	99.30 \pm 0.28	99.58 \pm 0.24	99.63 \pm 0.21	99.68 \pm 0.18	99.70\pm0.18	98.68 \pm 0.49	98.08 \pm 0.83	99.59 \pm 0.18
	MAE	6.12 \pm 0.92	2.94 \pm 0.89	2.90 \pm 0.74	2.36 \pm 0.77	2.19 \pm 0.70	2.01 \pm 0.67	1.96\pm0.64	3.91 \pm 1.10	4.66 \pm 1.42	2.24 \pm 0.55
$R=16.0$	MSE	17.77 \pm 5.32	8.63 \pm 4.46	8.58 \pm 2.79	5.16 \pm 3.34	4.74 \pm 2.30	3.99 \pm 2.08	3.45\pm1.59	11.66 \pm 7.68	13.02 \pm 7.84	5.34 \pm 2.24
	PSNR	38.34 \pm 2.22	40.92 \pm 1.43	41.35 \pm 2.47	43.72 \pm 2.64	43.79 \pm 2.17	44.65 \pm 2.39	45.16\pm2.15	40.57 \pm 2.49	39.86 \pm 2.53	43.23 \pm 2.06
	SSIM	93.71 \pm 1.59	97.44 \pm 0.93	97.74 \pm 0.52	98.65 \pm 0.53	98.53 \pm 0.54	98.83 \pm 0.44	98.87\pm0.45	96.92 \pm 1.29	96.78 \pm 1.34	97.84 \pm 0.71
	MAE	8.79 \pm 1.61	6.11 \pm 1.19	5.88 \pm 1.66	4.77 \pm 1.56	4.64 \pm 1.24	4.24 \pm 1.23	4.02\pm1.05	6.27 \pm 1.76	6.28 \pm 1.94	5.33 \pm 1.23

TABLE II

GENERALIZATION RESULTS ON THE CMRxRECON DATASET (MEAN \pm STANDARD DEVIATION).

Metrics	Compressed-Sensing			Supervised				Unsupervised			
	ℓ_2 -StoRM	L+S	k-t SLR	CRNN	SLR-net	CTF-net	L+S-net	TDIP	Gen-StoRM	GIP	
$R=8.0$	MSE	4.93 \pm 4.60	2.26 \pm 2.10	2.11 \pm 1.71	1.75 \pm 1.62	1.26 \pm 0.62	1.08 \pm 0.66	1.43 \pm 2.28	5.73 \pm 2.74	10.06 \pm 7.35	0.87\pm0.34
	PSNR	43.87 \pm 2.27	47.15 \pm 2.03	47.35 \pm 1.92	48.34 \pm 2.23	49.43 \pm 1.83	50.21 \pm 1.98	49.67 \pm 2.51	43.05 \pm 1.83	40.86 \pm 2.40	50.90\pm1.62
	SSIM	97.71 \pm 0.96	99.06 \pm 0.25	99.18 \pm 0.18	99.31 \pm 0.25	99.41 \pm 0.18	99.50 \pm 0.16	99.46 \pm 0.20	97.82 \pm 0.56	96.36 \pm 1.99	99.53\pm0.13
	MAE	4.71 \pm 1.42	3.14 \pm 0.92	3.04 \pm 0.81	2.91 \pm 0.82	2.59 \pm 0.56	2.37 \pm 0.55	2.56 \pm 0.97	5.10 \pm 1.10	6.45 \pm 2.13	2.18\pm0.42
$R=16.0$	MSE	11.67 \pm 14.47	7.00 \pm 6.66	6.20 \pm 6.00	6.60 \pm 3.99	5.97 \pm 3.50	5.37 \pm 3.85	4.84 \pm 2.69	9.99 \pm 4.54	14.75 \pm 8.55	3.33\pm1.37
	PSNR	40.23 \pm 2.31	42.39 \pm 2.36	42.94 \pm 2.35	43.09 \pm 2.38	42.81 \pm 2.10	43.76 \pm 2.21	43.68 \pm 2.02	40.67 \pm 1.98	39.11 \pm 2.30	45.12\pm1.66
	SSIM	95.37 \pm 1.79	97.54 \pm 0.76	97.88 \pm 0.70	98.08 \pm 0.75	97.98 \pm 0.57	98.24 \pm 0.77	98.22 \pm 0.49	96.76 \pm 0.85	95.35 \pm 2.26	98.44\pm0.40
	MAE	6.97 \pm 2.36	5.34 \pm 1.71	4.91 \pm 1.56	5.14 \pm 2.02	5.16 \pm 1.24	4.73 \pm 1.64	4.73 \pm 1.10	6.34 \pm 1.36	7.52 \pm 2.21	4.21\pm0.84

CNN generators G_i are used for reconstruction. “DIP+GCN” means utilizing the whole G_θ network for reconstruction by directly fitting the k -space data. “DIP+ADMM” means the CNN generators are used for reconstruction with the ADMM algorithm, in which the G_θ is substituted by G_i . We also saved the intermediate results of different ADMM iterations to visualize the optimization process.

The results of the ablation study are shown in Figure 6. The “DIP only” approach can eliminate the undersampling artifacts to some extent; however, the reconstructed images exhibit significant blurring and artifacts. The “DIP+GCN” strategy utilizes the GCN to exploit the spatio-temporal correlations, significantly enhancing the reconstruction accuracy.

The “DIP+ADMM” method employs the ADMM optimization algorithm to leverage the structured priors of DIP, leading to improved reconstruction performance; however, its effectiveness is inferior to “DIP+GCN”. Our proposed GIP method synergistically incorporates DIP, GCN, and the ADMM optimizer into one algorithm, achieving the highest reconstruction fidelity. Table IV summarizes the quantitative results of the ablation study, corroborating the contribution of each component in GIP to the ultimate reconstruction performance.

TABLE III

THE COMPUTATIONAL TIME OF DIFFERENT METHODS ON GPU.

	ℓ_2 -StoRM	L+S	k-t SLR	CRNN	SLR-net	CTF-net	L+S-net	TDIP	Gen-StoRM	GIP
Train	/	/	/	16.2 h	5.8 h	28.9 h	4.2 h	/	/	/
Recon	5.1 s	9.6 s	32.2 s	0.43 s	0.12 s	0.91 s	0.09 s	58.6 min	37.9 min	172.4 min

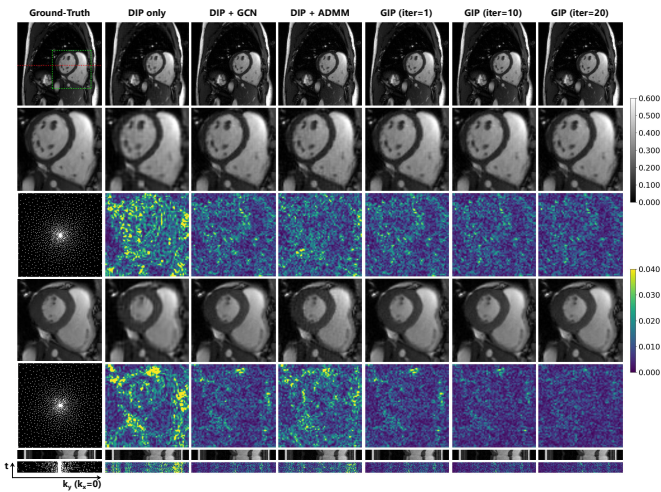


Fig. 6. Illustration of the ablation study results. From left to right columns are the ground truth and the reconstruction results by “DIP only”, “DIP+GCN”, “DIP+ADMM” and the proposed GIP method with 1, 10, and 20 iterations. The diastolic frames are displayed on the second row, and the third row displays the corresponding error maps. The results of the systolic frames are shown in the fourth and fifth row. The y -t motion profiles and error maps are shown at the bottom.

TABLE IV

		QUANTITATIVE RESULTS OF THE ABLATION STUDY.					
Metrics		DIP only	DIP + GCN	DIP + ADMM	GIP (iter=1)	GIP (iter=10)	GIP (iter=20)
R=8.0	MSE	23.91±8.15	2.59±0.96	5.67±1.62	1.44±0.62	1.17±0.50	0.98±0.45
	PSNR	36.52±1.36	46.23±1.70	42.69±1.27	48.93±2.01	49.83±1.97	50.63±2.08
	SSIM	94.20±0.98	99.05±0.34	97.64±0.40	99.40±0.23	99.51±0.19	99.59±0.18
	MAE	10.09±1.72	3.68±0.79	5.53±0.83	2.74±0.64	2.45±0.57	2.24±0.55
R=16.0	MSE	32.95±8.26	8.70±3.61	19.46±5.63	7.67±3.26	5.73±2.53	5.34±2.24
	PSNR	35.03±1.17	41.08±2.01	37.33±1.29	41.66±2.08	42.99±2.19	43.23±2.06
	SSIM	91.08±1.41	97.04±0.96	92.58±1.27	97.22±0.88	97.85±0.75	97.84±0.71
	MAE	12.27±1.78	6.64±1.56	10.14±1.52	6.24±1.48	5.42±1.34	5.33±1.23

VI. DISCUSSION

A. Analysis of the GIP Model

Previous studies have shown that the DIP generator structure is critical to its regularization effect [43]. In static image restoration, most works adopt a pyramid-shaped CNN generator and a Gaussian noise input [21] [44], which is demonstrated to be asymptotically equivalent to a stationary Gaussian process prior [45]. However, dynamic images have a key distinction that there exist strong correlations between the frames. Existing methods for dynamic MRI reconstruction employ a shared CNN across frames and express the correlations as the proximity between the latent variables [23] [24]. Since the latent variables lack image structure, this model cannot fully exploit the spatio-temporal redundancies within the dynamic data. In comparison, GIP exchanges the generative order by first recovering the image structure and then modeling the correlations within the feature space. The major drawback of this model is the rapid expansion of model complexity. Inspired by ℓ_2 -SToRM, we adopt the graph model in the feature space to reduce the model complexity from quadratic to linear with the frame number. We designed a GCN to adaptively learn the graph structure and generate dynamic images through graph convolution, enabling a flexible and expressive representation for general dynamic imaging problems. Although better modeling strategies may be proposed in the future, we demonstrate that the simple frame-as-node model can significantly improve the reconstruction performance.

B. Benefit of the Alternated Optimization Algorithm

Despite the good regularization effect of DIP, CNN can also introduce a strong bias to the output images. It is well-

known that images reconstructed by a pure CNN architecture tend to lose image texture and details [46]. For this reason, directly fitting the k -space often causes over-smoothing in the reconstructed images. Therefore, it is necessary to decouple image reconstruction from the constraints of the network structural prior. In this work, we devise an ADMM algorithm to alternately optimize network parameters and images, which allows us to update the images and priors synergistically, and control the contribution of the network’s output to the reconstruction results. Although the optimization objective is a non-convex problem, experimental results show that the optimization algorithm still has a good convergence property, and can significantly improve the reconstruction performance compared with directly fitting the k -space data.

C. Limitations and Future Directions

The proposed GIP method still has some limitations that need to be addressed in future research. The first is the long reconstruction time. Since the ADMM algorithm alternately optimizes the image and the network parameters, each iteration requires a separate network training. In this work, we fix the training iterations as 500, leading to a reconstruction time of about one hour for a single slice. Besides, the pretraining of the GIP generator takes approximately two hours. Possible solutions may include exploring the optimal iteration numbers, seeking better pretraining strategies, and designing accelerated optimization algorithms to shorten the reconstruction time. The second problem is the linear growth of the GIP model. Because GIP assigns an independent set of weights for each node, the model size and memory consumption are proportional to the number of frames. Therefore, GIP is mainly suitable for reconstruction problems with fewer frames, such as the gated dynamic MRI. For real-time dynamic imaging of a long period, the computational resource demand of the GIP model may become unacceptable. An interesting direction for future research could be designing a compromise model between the single-generator scheme and the GIP model, making a balance between resource consumption and model expression ability. Finally, this article mainly validates the GIP method in cardiac cine MRI reconstruction. Since cardiac cine MRI data is relatively easy to obtain, supervised deep learning methods have an absolute advantage in terms of reconstruction accuracy and speed. However, in more challenging scenarios such as 4D blood flow imaging, it is very difficult to obtain high-quality training data. It is valuable to investigate the effectiveness of GIP in other dynamic imaging applications in the future.

VII. CONCLUSION

In this work, we propose an unsupervised method for dynamic cine MRI reconstruction named Graph Image Prior (GIP). This work introduces a new methodology of generative modeling, which first recovers the image structure and then models the spatio-temporal manifold in the feature space. We adopt a frame-as-graph-node model to parameterize the feature space and utilize a GCN to exploit the spatio-temporal correlations. Besides, we also devise an ADMM algorithm which alternately optimizes the images and network parameters. This method displays significant improvements in reconstruction accuracy, and is promising for other reconstruction applications where fully-sampled data is scarce or unavailable.

REFERENCES

- [1] J. Tsao, P. Boesiger, and K. P. Pruessmann, "k-t blast and k-t sense: dynamic mri with high frame rate exploiting spatiotemporal correlations," *Magnetic Resonance in Medicine: An Official Journal of the International Society for Magnetic Resonance in Medicine*, vol. 50, no. 5, pp. 1031–1042, 2003.
- [2] Z.-P. Liang, "Spatiotemporal imaging with partially separable functions," in *2007 4th IEEE international symposium on biomedical imaging: from nano to macro*. IEEE, 2007, pp. 988–991.
- [3] L. Feng, M. B. Srichai, R. P. Lim, A. Harrison, W. King *et al.*, "Highly accelerated real-time cardiac cine mri using k-t sparse-sense," *Magnetic resonance in medicine*, vol. 70, no. 1, pp. 64–74, 2013.
- [4] H. Jung, K. Sung *et al.*, "k-t focuss: a general compressed sensing framework for high resolution dynamic mri," *Magnetic Resonance in Medicine: An Official Journal of the International Society for Magnetic Resonance in Medicine*, vol. 61, no. 1, pp. 103–116, 2009.
- [5] B. Zhao, J. P. Haldar, A. G. Christodoulou, and Z.-P. Liang, "Image reconstruction from highly undersampled (k, t)-space data with joint partial separability and sparsity constraints," *IEEE transactions on medical imaging*, vol. 31, no. 9, pp. 1809–1820, 2012.
- [6] S. G. Lingala, Y. Hu, E. DiBella, and M. Jacob, "Accelerated dynamic mri exploiting sparsity and low-rank structure: kt slr," *IEEE transactions on medical imaging*, vol. 30, no. 5, pp. 1042–1054, 2011.
- [7] R. Otazo, E. Candes, and D. K. Sodickson, "Low-rank plus sparse matrix decomposition for accelerated dynamic mri with separation of background and dynamic components," *Magnetic resonance in medicine*, vol. 73, no. 3, pp. 1125–1136, 2015.
- [8] S. Poddar and M. Jacob, "Dynamic mri using smoothness regularization on manifolds (storm)," *IEEE transactions on medical imaging*, vol. 35, no. 4, pp. 1106–1115, 2015.
- [9] U. Nakarmi, Y. Wang, J. Lyu, D. Liang, and L. Ying, "A kernel-based low-rank (klr) model for low-dimensional manifold recovery in highly accelerated dynamic mri," *IEEE transactions on medical imaging*, vol. 36, no. 11, pp. 2297–2307, 2017.
- [10] J. Lyu, C. Qin, S. Wang, F. Wang, Y. Li, Z. Wang *et al.*, "The state-of-the-art in cardiac mri reconstruction: Results of the cmrxcon challenge in miccai 2023," *arXiv preprint arXiv:2404.01082*, 2024.
- [11] J. Sun, H. Li, Z. Xu *et al.*, "Deep admm-net for compressive sensing mri," *Advances in neural information processing systems*, vol. 29, 2016.
- [12] H. K. Aggarwal, M. P. Mani, and M. Jacob, "Modl: Model-based deep learning architecture for inverse problems," *IEEE transactions on medical imaging*, vol. 38, no. 2, pp. 394–405, 2018.
- [13] K. Hammernik, T. Klatzer, E. Kobler, M. P. Recht *et al.*, "Learning a variational network for reconstruction of accelerated mri data," *Magnetic resonance in medicine*, vol. 79, no. 6, pp. 3055–3071, 2018.
- [14] J. Schlemper, J. Caballero, J. V. Hajnal, A. N. Price, and D. Rueckert, "A deep cascade of convolutional neural networks for dynamic mr image reconstruction," *IEEE transactions on Medical Imaging*, vol. 37, no. 2, pp. 491–503, 2017.
- [15] C. Qin, J. Schlemper, J. Caballero, A. N. Price, J. V. Hajnal, and D. Rueckert, "Convolutional recurrent neural networks for dynamic mr image reconstruction," *IEEE transactions on medical imaging*, vol. 38, no. 1, pp. 280–290, 2018.
- [16] C. Qin, J. Duan, K. Hammernik, J. Schlemper, T. Küstner, R. Botnar, C. Prieto, A. N. Price *et al.*, "Complementary time-frequency domain networks for dynamic parallel mr image reconstruction," *Magnetic Resonance in Medicine*, vol. 86, no. 6, pp. 3274–3291, 2021.
- [17] J. Zhang and B. Ghanem, "Ista-net: Interpretable optimization-inspired deep network for image compressive sensing," in *Proceedings of the IEEE conference on computer vision and pattern recognition*, 2018, pp. 1828–1837.
- [18] Z. Ke, W. Huang, Z.-X. Cui, J. Cheng, S. Jia, H. Wang, X. Liu, H. Zheng, L. Ying *et al.*, "Learned low-rank priors in dynamic mr imaging," *IEEE Transactions on Medical Imaging*, vol. 40, no. 12, pp. 3698–3710, 2021.
- [19] W. Huang, Z. Ke, Z.-X. Cui, J. Cheng, Z. Qiu, S. Jia, L. Ying, Y. Zhu, and D. Liang, "Deep low-rank plus sparse network for dynamic mr imaging," *Medical Image Analysis*, vol. 73, p. 102190, 2021.
- [20] D. Ulyanov, A. Vedaldi, and V. Lempitsky, "Deep image prior," in *Proceedings of the IEEE conference on computer vision and pattern recognition*, 2018, pp. 9446–9454.
- [21] M. Z. Darestani and R. Heckel, "Accelerated mri with un-trained neural networks," *IEEE Transactions on Computational Imaging*, vol. 7, pp. 724–733, 2021.
- [22] K. Gong, C. Catana, J. Qi, and Q. Li, "Pet image reconstruction using deep image prior," *IEEE transactions on medical imaging*, vol. 38, no. 7, pp. 1655–1665, 2018.
- [23] J. Yoo, K. H. Jin, H. Gupta, J. Yerly, M. Stuber, and M. Unser, "Time-dependent deep image prior for dynamic mri," *IEEE Transactions on Medical Imaging*, vol. 40, no. 12, pp. 3337–3348, 2021.
- [24] Q. Zou, A. H. Ahmed, P. Nagpal, S. Kruger, and M. Jacob, "Dynamic imaging using a deep generative storm (gen-storm) model," *IEEE transactions on medical imaging*, vol. 40, no. 11, pp. 3102–3112, 2021.
- [25] A. H. Ahmed, Q. Zou, P. Nagpal, and M. Jacob, "Dynamic imaging using deep bi-linear unsupervised representation (deblur)," *IEEE transactions on medical imaging*, vol. 41, no. 10, pp. 2693–2703, 2022.
- [26] Y. Q. Mohsin, S. Poddar, and M. Jacob, "Free-breathing & gated cardiac mri using iterative storm (i-storm)," *IEEE transactions on medical imaging*, vol. 38, no. 10, pp. 2303–2313, 2019.
- [27] S. Poddar, Y. Q. Mohsin, D. Ansah, B. Thattaliyath, R. Ashwath, and M. Jacob, "Manifold recovery using kernel low-rank regularization: Application to dynamic imaging," *IEEE transactions on computational imaging*, vol. 5, no. 3, pp. 478–491, 2019.
- [28] U. Nakarmi, K. Slavakis, and L. Ying, "Mls: Joint manifold-learning and sparsity-aware framework for highly accelerated dynamic magnetic resonance imaging," in *2018 IEEE 15th International Symposium on Biomedical Imaging (ISBI 2018)*. IEEE, 2018, pp. 1213–1216.
- [29] S. Biswas, H. K. Aggarwal, and M. Jacob, "Dynamic mri using model-based deep learning and storm priors: Modl-storm," *Magnetic resonance in medicine*, vol. 82, no. 1, pp. 485–494, 2019.
- [30] Z. Wu, S. Pan, F. Chen, G. Long, C. Zhang, and S. Y. Philip, "A comprehensive survey on graph neural networks," *IEEE transactions on neural networks and learning systems*, vol. 32, no. 1, pp. 4–24, 2020.
- [31] A. Sandryhaila *et al.*, "Discrete signal processing on graphs," *IEEE transactions on signal processing*, vol. 61, no. 7, pp. 1644–1656, 2013.
- [32] M. Defferrard, X. Bresson, and P. Vandergheynst, "Convolutional neural networks on graphs with fast localized spectral filtering," *Advances in neural information processing systems*, vol. 29, 2016.
- [33] T. N. Kipf and M. Welling, "Semi-supervised classification with graph convolutional networks," *arXiv preprint arXiv:1609.02907*, 2016.
- [34] G. Li, M. Muller, A. Thabet, and B. Ghanem, "Deepgcns: Can gcns go as deep as cnns?" in *Proceedings of the IEEE/CVF international conference on computer vision*, 2019, pp. 9267–9276.
- [35] K. Han, Y. Wang, J. Guo, Y. Tang, and E. Wu, "Vision gnn: An image is worth graph of nodes," *Advances in Neural Information Processing Systems*, vol. 35, pp. 8291–8303, 2022.
- [36] F. Cheng, Y. Liu, Y. Chen, and P.-T. Yap, "High-resolution 3d magnetic resonance fingerprinting with a graph convolutional network," *IEEE transactions on medical imaging*, vol. 42, no. 3, pp. 674–683, 2022.
- [37] H. Lu, H. Ye, L. L. Wald, and B. Zhao, "Accelerated mr fingerprinting with low-rank and generative subspace modeling," *arXiv preprint arXiv:2305.10651*, 2023.
- [38] C. Chen, Y. Liu, P. Schniter, M. Tong, R. Ahmad *et al.*, "Ocmr (v1.0)—open-access multi-coil k-space dataset for cardiovascular magnetic resonance imaging," *arXiv preprint arXiv:2008.03410*, 2020.
- [39] T. Zhang, J. M. Pauly, S. S. Vasanawala, and M. Lustig, "Coil compression for accelerated imaging with cartesian sampling," *Magnetic resonance in medicine*, vol. 69, no. 2, pp. 571–582, 2013.
- [40] C. Wang, J. Lyu, S. Wang, C. Qin, K. Guo, X. Zhang, J. Jin *et al.*, "Cmrxcon: an open cardiac mri dataset for the competition of accelerated image reconstruction," *arXiv preprint arXiv:2309.10836*, 2023.
- [41] M. Uecker, P. Lai, M. J. Murphy, P. Virtue, M. Elad, J. M. Pauly, S. S. Vasanawala, and M. Lustig, "Espirit—an eigenvalue approach to autocalibrating parallel mri: where sense meets grappa," *Magnetic resonance in medicine*, vol. 71, no. 3, pp. 990–1001, 2014.
- [42] Z. Wang, A. C. Bovik, H. R. Sheikh, and E. P. Simoncelli, "Image quality assessment: from error visibility to structural similarity," *IEEE transactions on image processing*, vol. 13, no. 4, pp. 600–612, 2004.
- [43] M. E. Arican, O. Kara, G. Bredell, and E. Konukoglu, "Isnas-dip: Image-specific neural architecture search for deep image prior," in *Proceedings of the IEEE/CVF Conference on Computer Vision and Pattern Recognition*, 2022, pp. 1960–1968.
- [44] R. Heckel and P. Hand, "Deep decoder: Concise image representations from untrained non-convolutional networks," *arXiv preprint arXiv:1810.03982*, 2018.
- [45] Z. Cheng, M. Gadelha, S. Maji, and D. Sheldon, "A bayesian perspective on the deep image prior," in *Proceedings of the IEEE/CVF Conference on Computer Vision and Pattern Recognition*, 2019, pp. 5443–5451.
- [46] G. Yang, S. Yu, H. Dong, G. Slabaugh, P. L. Dragotti, X. Ye, F. Liu, S. Arridge *et al.*, "Dagan: Deep de-aliasing generative adversarial networks for fast compressed sensing mr reconstruction," *IEEE transactions on medical imaging*, vol. 37, no. 6, pp. 1310–1321, 2017.